# SIMULATING GRAIN SIZE ESTIMATION

## IVAN SAXL[1]*, KATARÍNA SÜLLEIOVÁ[2], PETR PONÍŽIL[3]

3D Voronoi tessellations generated by four point processes with widely different cell size distributions have been chosen as the models of the polycrystalline grain structure. Simulated planar and line sections have been then examined by manual analysis and by computerized analogy of automatic image analysis. The grain size estimation procedures recommended by the ASTM Standards are compared with the known values obtained by medium scale stochastic simulations. Finally, a new approximate method of estimating the mean grain volume is proposed.

K e y   w o r d s: grain size estimation, ASTM Standards, Voronoi tessellations, computer simulation

## SIMULACE ODHADU VELIKOSTI ZRNA

Prostorové Voronoiovy teselace generované čtyřmi bodovými procesy s výrazně rozdílným rozdělením velikosti cel byly vybrány jako modely zrn polykrystalu. Počítačově simulované rovinné a lineární řezy byly pak proměřeny jednak manuálně, jednak počítačově simulovanou analogií automatické obrazové analýzy. Metody odhadu velikosti zrna doporučené ASTM byly porovnány s hodnotami získanými počítačovými simulacemi středního rozsahu. Závěrem je navržena metoda zpřesnění těchto odhadů.

## 1. Introduction

3D grain size estimation from a partial information available by examining planar or line section of opaque materials is an important problem in science as well as in technical practice. In the latter case, the national standards more or less similar to the ASTM E-112 standards (see [1]) are obligatory whereas more sophisticated methods based on various approximate relations are used in research laboratories (for a review see [2]). However, the both approaches include several assumptions concerning shape and size distributions of space filling grains which

[1]  Mathematical Institute, Acad. Sci. of the Czech Republic, Žitná 25, CZ-115 67 Praha 1, Czech Republic
[2]  Institute of Materials Research, Slovak Academy of Sciences, SK-043 53 Košice, Watsonova 47, Slovak Republic
[3]  Tomas Bata University, náměstí TGM 275, CZ-762 72 Zlín, Czech Republic
*  corresponding author, e-mail: `saxl@math.cas.cz`

are usually only vaguely stated and their justification is, in general, hardly possible. A peculiar feature of this topic is that even a completely unrealistic assumptions (e.g. that all grain profiles are congruent circles or all profile chords are isotropic uniform random chords of a system of congruent balls) can sometimes lead to reasonable conclusions valid in a wide range of grain structures occurring in practice. Nevertheless, leaving aside 3D probes of the disector type [3], the true 3D grain structure can never be completely restored and, consequently, the outcome of the estimation based on planar or line data is always doubtful.

Stochastic simulations suggest a unique possibility to tackle the problem from another side. First a model of grain structure – a spatial tessellation [4] – is generated and its planar and line sections (2D and 1D tessellations induced by the original 3D tessellation) are constructed. Then the geometrical properties of all these three tessellations are determined with a sufficient accuracy. As the first approximation of grain structures, the well known Voronoi tessellations formed by polygonal convex cells can be used. An extensive database of Voronoi cell properties has been created by the authors and is exposed on the Internet [5]. It includes regular isohedral tessellations formed by translation equivalent cells (the term *tiling* instead of *tessellation* is usually used in this case) as well as multimodal cell systems generated by point cluster fields. Consequently, everything is known here and the acceptability of various approximate relations between the original and induced tessellations can be simply verified. A simple graphical tool – $w$-$s$ diagram – was devised in order to illustrate the relations between the original and induced cell properties and is described at length in [6].

Whereas samples of considerable size (typically $\approx 10^3$ realizations with $\approx 10^3$ cells in each of them) were used to compute the above mentioned database, much smaller samples of several hundreds of profiles at most are usually available for either manual or automatic (image) analysis of real material sections and, moreover, the measurement error cannot be in either case neglected. The purpose of the present paper is to compare the results obtained by medium-scale simulation with those ones acquired by manual analysis of computer generated section images and by a somewhat artificial computerized model of the high resolution automatic image analysis.

## 2. Simulated tessellations

The Voronoi tessellations of various kind are generated from a point pattern $X = \{x\}$ by adjoining to any of its point $x$ a union (called the cell) of all points $y$ of the embedding space that lie closer to $x$ than to any other point of the pattern; the boundary of the cell is formed by points $y$ with the same spacing to more than one point of $X$. The most important cell (grain) size characteristics are cell volume $v$, surface $s$, mean breadth $w$ (also the mean calliper or Feret diameter), induced cell (profile) area $a$, and chord (intercept) length $l$. Tessellation intensities or

densities (the mean numbers of features per unit content of the space) are $\lambda = 1/\mathbf{E}v$ for grains, $\lambda' = 1/\mathbf{E}a$ for profiles, $\lambda'' = 1/\mathbf{E}l$ for chords. Their estimators are $[\lambda'] = N_A$, $[\lambda''] = N_L$, where $N_A$ is the number of observed profiles per unit area of a section plane and $N_L$ is the number of profile chords per unit length of a test line.

Four point patterns (frequently called the point processes or point fields [7]) have been selected in the present study. The first of them is derived from the face-centred cubic lattice by giving to any its point an independent identically distributed (i.i.d.) random shift – hence the term *displaced lattice*. The shift distribution is 3D normal $N(0, \Sigma^2)$, $\Sigma^2 = u^2 \mathcal{I}$, where $\mathcal{I}$ is the unit matrix. The choice of $u = 0.2$ (in the units of the nearest neighbour distance of lattice points) produces the tessellation in which the cells of the originally isohedral tiling by rhombic dode-cahedrons are heavily randomly corrugated. The tessellation is denoted by Bcf-0.2 (Bcf means **B**ookstein model [8] on a **c**ubic **f**ace centred lattice).

The second grain structure model is the Poisson-Voronoi tessellation (PVT) generated by the stationary Poisson point process (PPP), which is roughly speaking a limit case of a uniform random arrangement of points on a bounded area.

Two remaining processes are point cluster fields based on PPP. Let the point cluster be a random bounded $n$-tuple of points with $n$ being Poisson distributed with the mean $\mathbf{E}n = N$; the cluster is called *globular* (G) if the points are distributed uniformly at random within a ball of diameter $\gamma$ and *spherical* (S) if they lie only on the ball surface ($\gamma$ is usually given in the units of the mean nearest neighbour distance $\rho_p$ of the parent process) [9]. Let now be any point of the parent PPP replaced by a random cluster with a probability $0 \le p \le 1$. The resulting point process will be called the *Bernoulli cluster field* [10]. The choice of $p = 1$ produces a standard Neyman-Scott process [7], whereas the original PPP results if $p = 0$. The choice $p = 1$, $\gamma = 2$ and $N = 30$ gives rather large dissolved intermixed clusters – the notation is PG30. The distribution of the cell volume in the resulting tessellations is mildly bimodal with the ratio of modes 1:8 [9]. The last tessellation is generated by the Bernoulli cluster field with $p = 0.5$, $\gamma = 0.05$, $N = 70$ and spherical clusters – BePS70. The tessellation then consists of a 1:1 mixture of large, slightly corrugated parent cells and of such cells fragmented into $n$ small elongated and wedge-like pieces. The distribution of the cell volume is again roughly bimodal with the mode ratio 1:70 (see [10]).

Selected characteristics of examined 3D tessellations and their induced 2D and 1D tessellations are shown in Table 1 (denoted by "sim"). They have been obtained by medium size ($10^5 \div 10^6$ cells or profiles) computer simulations – for details see [5, 9]. All tessellations are unit and the differences in the mean profile areas $\mathbf{E}a$ and chord lengths $\mathbf{E}w$ are small. On the other hand, the covered ranges of coefficients of variation are quite considerable: the ratios of the smallest to the highest values are about 1:23 for CV $v$ and roughly about 1:4 for CV $a$ and 1:2 for CV $l$.
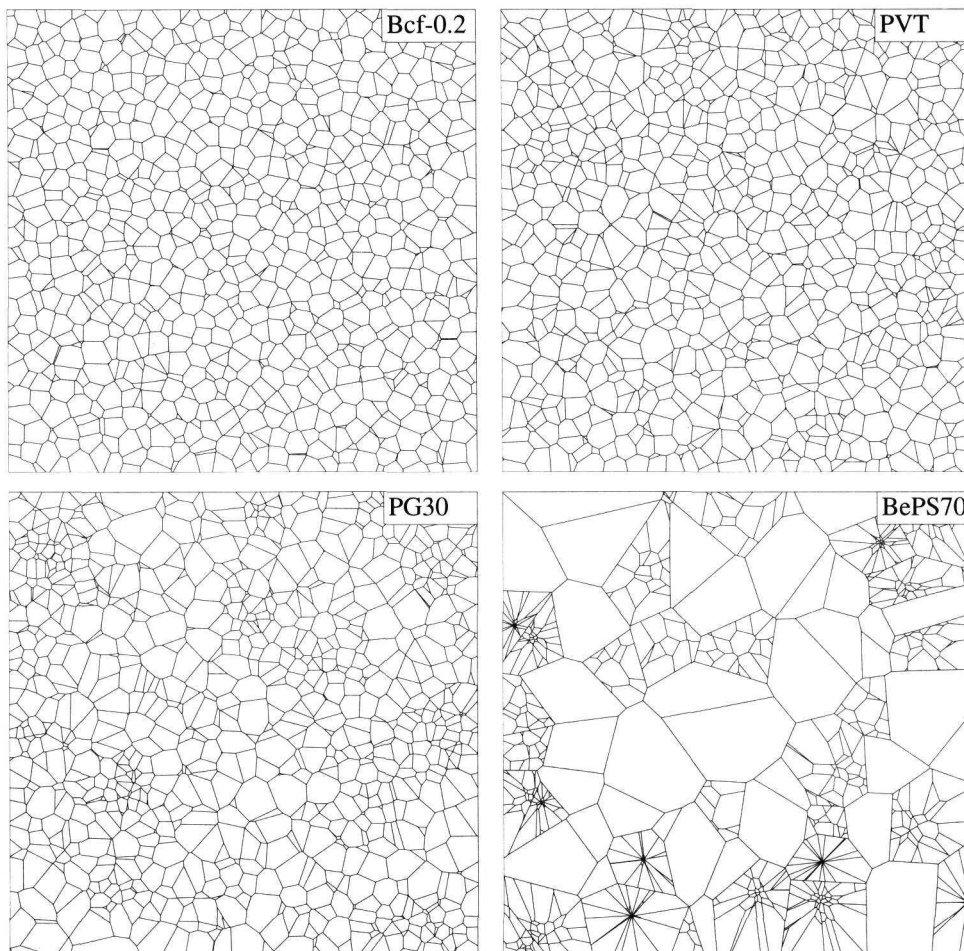
Fig. 1. Planar sections of examined 3D tessellations selected for simultaneous computer (profile area evaluation) and manual analysis (profile count and intercept length measurement). Four such samples of BePS70 were analysed in order to suppress their insufficient homogeneity.

The differences in coefficients of variation are drastically reduced in induced tessellations; nevertheless they are still much greater than the differences in the mean values of profile characteristics which are usually the exclusive object of estimation in technical practice. The planar sections of the four examined 3D tessellations are presented in Fig. 1, several features of tessellations mentioned above are discernible there.

T a b l e  1. Estimated values of induced tessellation characteristics obtained by simulation (sim.) and by manual and computerized analyses (bold)

| Not. | Type | $CV\,v$ | $\mathbf{E}a$ $[\mathbf{E}a]_{N_A}$ | $CV\,a$ $[CVa]_a$ | $[\mathbf{E}a]_{N_A}$ | $\mathbf{E}l$ $[\mathbf{E}l]_{N_L}$ | $CV\,l$ $[CV\,l]_l$ | $c$ $[c]_{N_A,N_L}$ |
|------|------|------|------|------|------|------|------|------|
| A | Bcf-0.2 sim. | 0.20 | 0.70 | 0.60 | – | 0.71 | 0.53 | 0.72 |
|   | measured | – | **0.71** | **0.63** | 0.75 | 0.73 | 0.46 | 0.71 |
| B | PVT sim. | 0.42 | 0.69 | 0.70 | – | 0.69 | 0.58 | 0.69 |
|   | measured | – | **0.72** | **0.76** | 0.77 | 0.69 | 0.56 | 0.62 |
| C | PG30 sim. | 1.10 | 0.72 | 0.99 | – | 0.71 | 0.67 | 0.70 |
|   | measured | – | **0.69** | **0.97** | 0.72 | 0.76 | 0.63 | 0.80 |
| D | BePS70 sim. | 4.50 | 0.67 | 2.72 | – | 0.77 | 1.15 | 0.88 |
|   | measured* | – | **0.91** | **2.52** | 0.78 | 0.89 | 1.04 | 0.91 |

\* four sections examined

## 3. Methods of estimation and results

In general, the recommendations of the ASTM E 112-82 "Standard methods for determining average grain size" have been followed. The number of profiles after the edge correction is $N_A = (n_1 + n_2/2 - 1)/W$, where $n_1$ is the number of profiles lying within the observing window of area $W$ and $n_2$ is the number of profiles intersecting the rectangle boundary. The tessellations have been produced in a unit cube, the expected number of generated points was 15 000 which is the volume of this cube in the scale of unit tessellations. The edge effect has been carefully removed and the measurement was made only in the inner part of the cube. The point processes based on PPP are isotropic, whereas random orientations of the displaced generating lattices with respect to cube orientation were chosen in the anisotropic case A. The planar sections are squares of the size 0.6×0.6 in the unit cube, or, of the area of $W = 219$ (in the units corresponding to $N_V = 1$). The sections shown in Fig. 1 have been analysed manually as well as directly in the computer by imitating the procedure of the automatic image analysis (see below) – the results are summarized in Table 1, where also the shortened notation A, B, C, D is introduced (the subscripts of the estimator brackets denote the experimentally accessible quantity used to obtain the estimate).

### a) Profile areas (Jeffries procedure)

The numbers of grains $n_1, n_2$ have been simultaneously determined by manual and computer analysis; the areas $a_i$ of individual profiles have also been estimated in the latter case. The estimator $[\lambda']_{N_A} = [1/\mathbf{E}a]_{N_A} = N_A$ was used in the both cases. The number of examined profiles was $W/\mathbf{E}a \sim 300$ per section and the coefficient of error CE of the estimated mean $\mathbf{E}a$ was then 0.06 $CV\,a$, i.e. 0.036 for the specimen A and 0.08 for specimen D with four examined sections.

Profile areas have been measured by means of a computerized image analysis (see below). In order to include also the profiles intersecting the boundary of the observing window, the areas $a_i'$ of incomplete profiles have been randomly paired and CV $a$ estimated as the mean value of sample coefficients of variation corresponding to 10 such random pairings (Table 1). ($[\mathbf{E}a]_{N_A} = 1/N_A$ is the estimator used in manual analysis). One such a random pairing was used to estimate also the probability density functions $f(x)$ of profile areas by means of Epanechnikov kernel estimator [8] with the band width $h = 0.25$ (Fig. 2).
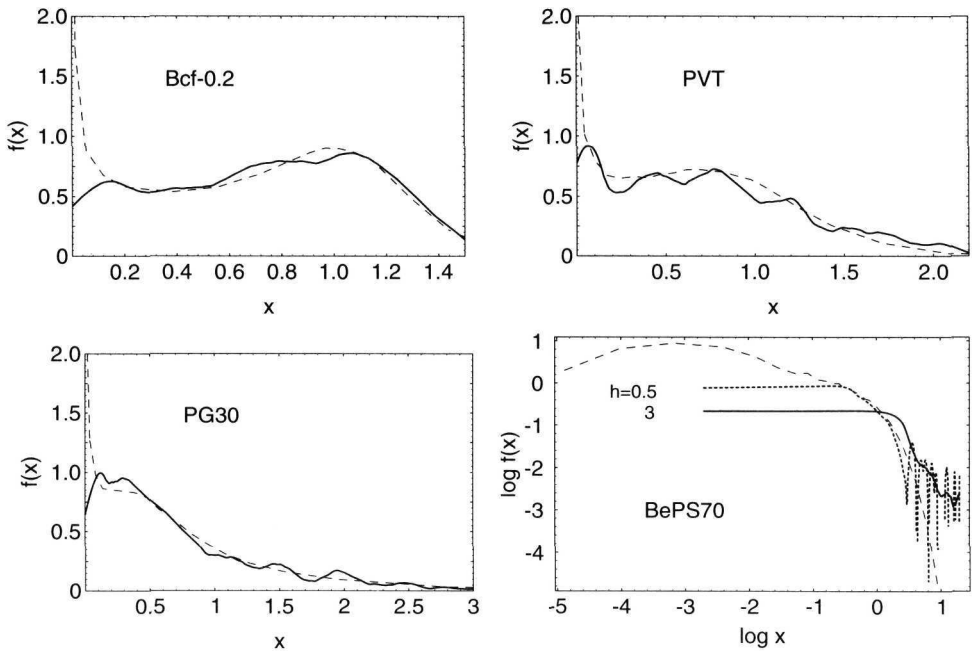


Fig. 2. Probability density functions $f(x)$ of the profile area $a$ in the section plane obtained by simulations (dashed) and kernel estimates of $f(x)$ obtained by computer evaluation of bitmaps of sections. Epanechnikov kernel estimator [8] with $h = 0.25$ was used for all cases but BePS70.

### b) Line intercepts (Heyn method)

The estimator $[\lambda'']_{N_L} = [1/\mathbf{E}l]_{N_L} = N_L$ was used and CV $l$ estimated by the sample coefficient of variation. Typically, about 140 chords per section were measured, thus giving the coefficient of error CE of the mean $\mathbf{E}l$ approximately $0.08\,\text{CV}\,l$ ($0.04\,\text{CV}\,l$ for the type D with four examined sections and 800 chords).

The edge effects have been excluded similarly as in the case of profile areas, namely the test lines crossing the whole observing window have been used and the

incomplete segments at the ends of test lines have been randomly paired. CV $l$ and the probability density function $f(x)$ of chord lengths have been estimated similarly (Fig. 3).
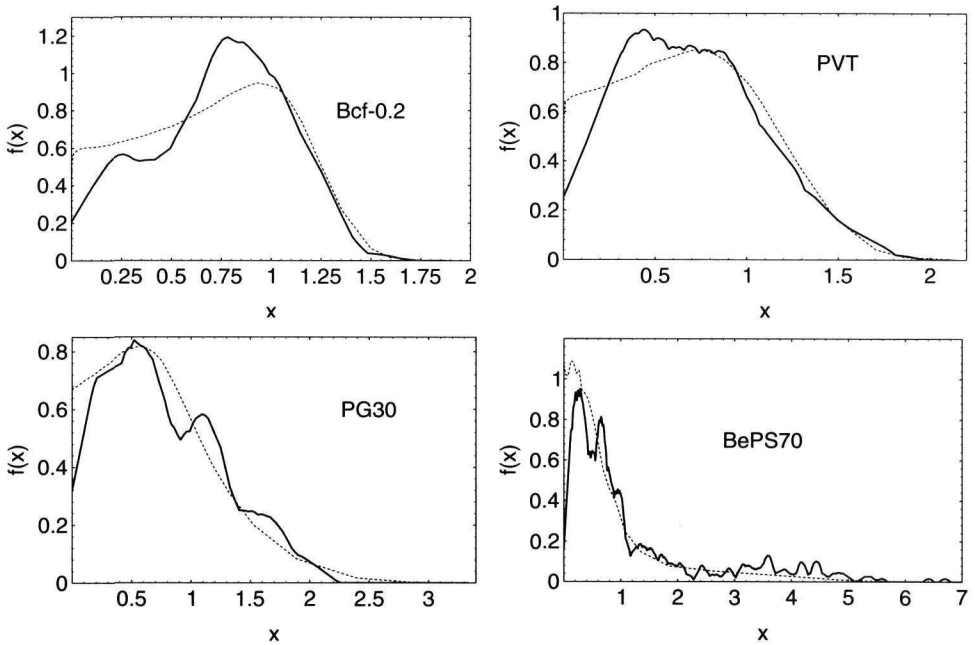


Fig. 3. Probability density functions $f(x)$ of the intercept length $l$ obtained by simulations (dotted) and kernel estimates of $f(x)$ obtained by manual linear intercept method (full line); Epanechnikov kernel estimator with the band width $h = 0.25$ [8].

### c) Computerized image analysis

The analysis was processed on simulated images of sections shown in Fig. 1, in the case of BePS70 other three planar sections have been added in order to suppress the large-scale inhomogeneity but even this turned out to be insufficient. Resolution of images was $6000 \times 6000$ pixels. The profile area was determined as the number $P$ of pixels forming the profile; the average number of pixels per profile was $\approx 1.2 \times 10^5$. The effect of the finite boundary trace thickness has been corrected by assuming that the measured profiles just fill the observing window. The numerical results are again in Table 1.

### d) Relation between $\lambda'$ and $\lambda''$ – factor c

The basic stereological equation (see e.g. [2, 7]) gives $\lambda' = c(\lambda'')^2$ with the scale invariant factor $c = \lambda^{-1}\mathbf{E}w/(\mathbf{E}s/4)^2$. Hence the factor $c$ can be calculated directly from simulations, estimated by $[c]_{N_L, N_A} = N_A/N_L^2$ and, finally, compared with the value $c_{\text{ASTM}} = 1/1.26 = 0.7937$ postulated by the ASTM Standards. Values of $c$ obtained by simulations and by manual analysis are shown in Table 1.

### e) Estimation of 3D cell intensity $\lambda$ – factors $c'$ and $c''$

The basic stereological equations (see e.g. [2, 7]) give two estimators of $\lambda$: $[\lambda]_{N_A} = c'N_A^{3/2}$ and $[\lambda]_{N_L} = c''N_L^3$, where the scale independent factors $c' = = 1/\sqrt{\lambda(\mathbf{E}w)^3}$ and $c'' = \lambda^{-2}(\mathbf{E}s/4)^{-3}$ can be calculated from simulations. They cannot be estimated from the sections and their theoretical values are known only for isohedral tilings by cells of given shape (tetrakaidecahedrons, rhombic dodeca-hedrons, cubes, hexagonal prisms etc.) and for few random tessellations (PVT, De-launey tessellation). ASTM Standards postulate $c' = 0.8$ (or 0.81) and $c'' = 0.57$, whereas CZ and SK Standards set $c' = 1$, $c'' = 0.7$. These values differ consid-erably from the correct values $c'_{\text{sim}}, c''_{\text{sim}}$ obtained by simulations (Table 2). The simulated as well as the ASTM recommended values are used to estimate the true spatial intensity $\lambda = 1$ from $N_A, N_L$ obtained by computerized image and manual analyses. The results are summarized in Table 2 (bold letters denote the estimates by computerized analysis).

T a b l e  2. Values of factors $c', c''$ obtained by simulations and estimated cell intensity of the unit 3D tessellations

| | $c'_{\text{sim}}$ | $[\lambda]_{N_A}$ | $[\lambda]_{N_A}^{\text{ASTM}}$ | $[\lambda]_{N_A}$ | $[\lambda]_{N_A}^{\text{ASTM}}$ | $c''_{\text{sim}}$ | $[\lambda]_{N_L}$ | $[\lambda]_{N_L}^{\text{ASTM}}$ |
|---|---|---|---|---|---|---|---|---|
| Bcf-0.2 | 0.591 | **0.99** | **1.36** | 0.91 | 1.25 | 0.36 | 0.91 | 1.44 |
| PVT | 0.568 | **0.93** | **1.33** | 0.99 | 1.41 | 0.33 | 0.84 | 1.45 |
| PG30 | 0.60 | **1.05** | **1.41** | 0.98 | 1.32 | 0.36 | 0.83 | 1.45 |
| BePS70* | 0.55 | **0.63** | **0.93** | 0.67 | 0.99 | 0.46 | 0.65 | 0.81 |

* four sections examined

### f) Estimation of CV v

The approximate relation $\text{CV}\,v = 0.948 + 1.464\ln(\text{CV}\,a)$ was proposed and tested in [2] to be valid for tessellations generated by displaced lattices and PS cluster fields. A similar relation for profile chords would be $\text{CV}\,v = 1.674 + +2.25\ln(\text{CV}\,l)$. The both relations are approximately valid only in a relatively narrow range $0.53 < \text{CV}\,a < 0.9$, $0.47 < \text{CV}\,l < 0.7$. The lower bounds of these in-tervals are the values corresponding to the isohedral tilings by tetrakaidecahedrons

Table 3. Estimated values of the coefficients of variation CV $v$

| Type | CV $v$ | $[\text{CV } v]_{\text{CV}_s a}$ | $[\text{CV } v]_{\text{CV}_c a}$ | $[\text{CV } v]_{\text{CV}_s l}$ | $[\text{CV } v]_{\text{CV}_m l}$ |
|------|--------|-----------|-----------|-----------|-----------|
| A | 0.20 | 0.20 | 0.27 | 0.24 | 0 |
| B | 0.42 | 0.43 | 0.55 | 0.45 | 0.37 |
| C | 1.1 | 0.93 | 0.90 | 0.77 | 0.56 |
| D | 4.5 | 2.40 | 2.30 | 1.98 | 1.76 |

(the Voronoi tessellation generated by the body-centred cubic lattice) and can be considered as the lowest attainable values of the coefficients of variation.

The estimates of CV $v$ shown in Table 3 were obtained by using these relations from $\text{CV}_s a$, $\text{CV}_s l$ obtained by simulations, from $\text{CV}_c a$ obtained by computerized analysis and from $\text{CV}_m l$ obtained by manual analysis.

## 4. Discussion

### a) w-s diagram

A useful tool of the analysis is the above-mentioned *w-s* diagram [6], the relevant section of which is shown in Fig. 4. Each tessellation is represented by
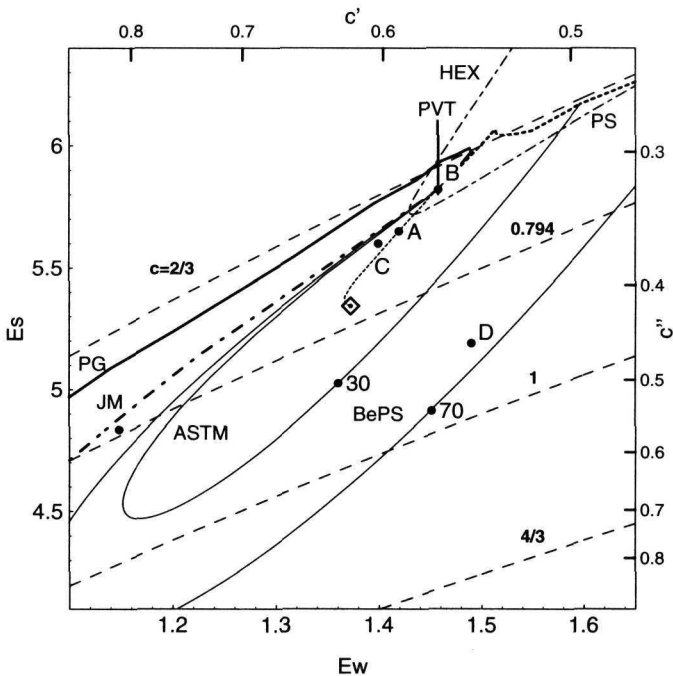


Fig. 4. A section of the *w-s* diagram containing examined and selected unit tessellations.

a point $[\mathbf{E}w, \mathbf{E}s]$. The isohedral tiling by rhombic dodecahedrons generated by the unit face-centred lattice is denoted by the diamond symbol near the centre of the figure and the dotted line joining it with the point representing the Poisson--Voronoi tessellation (denoted by PVT) represents Bookstein model on this lattice with $0 \leq u \leq 10$. Further, the dash-dotted line starting in the PVT point is the Johnson-Mehl model [11] with the variable nucleation intensity $I(t) = \alpha t^{\beta-1}$ (only the segment corresponding to $0 \leq \beta \leq 2.5$ is depicted). Thick diagonal line (full line denoted PG near its left end and dashed line denoted PS at its right end) describes tessellations generated by Poisson cluster fields; the cluster size is $\delta = 0.05$ in the units of the parent Poisson point process and the mean cluster cardinality is $1 \leq N \leq 40$ for globular clusters (PG) and $1 \leq N \leq 50$ for spherical (PS) clusters. The two loops lying below the figure diagonal are theoretical BePS tessellations with $\gamma = 0.05$, $N = 30, 70$ (see [10]). The shrinkage of loops takes place when $\gamma$ increases whereas they blow up moderately in the opposite case. The points denoted 30 and 70 show the positions of the tessellations with the maximum CV $v$, which correspond to the choice $p = 0.5$. The point corresponding to the ASTM is shown as the black circle at [1.15, 4.84]; the CZ and SK Standard point [1, 4.5] is out of the figure. The dashed net are the curves $c = $ const.

Moreover, the non-linear scale $c', c''$ with its own bold ticks is sketched. It was shown by Horálek [12] that the non-homogeneous Johnson-Mehl model with $\beta \approx 2$ approximately corresponds to the factors $c, c', c''$ postulated by ASTM. Finally, the examined tessellations are denoted by the black points and letters A, B, C, D (the values of $\mathbf{E}w, \mathbf{E}s$ obtained by simulations are used).

The inspection of the $w$-$s$ diagram illustrates the similarity between all considered tessellations in the values of the mean breadth $\mathbf{E}w$ but a distinct difference in the values of $\mathbf{E}s$ between the tessellations A, B, C (equiaxial cells) and D (flat, rod-like and wedge-like cells).

### b) Probability density functions of profile areas and chord lengths

The prominent feature of estimated pdf's (Figs. 2, 3) is the loss of small profiles. This deficit is perhaps more important in planar count. Fig. 3 shows that in contrast to a general belief, pdf's of profile area are *bimodal* with a very pronounced mode near zero. It corresponds to cell sections produced by section planes passing near cell vertices or edges which are nearly parallel to them. A rough estimate of this loss is about 6% for tessellations A, B, C and between 10 and 20% for BePS70 (even when several sections are combined in this case). The large inhomogeneity of BePS70 sections is perhaps responsible for such a large loss of small profiles that would be otherwise hardly acceptable in computerized analysis with such a high resolution power. In the two isotropic cases B, C, a substantial improvement would be achieved by increasing the number of measured features. However, one goal of the present analysis is to show that rather reliable

estimates of pdf's are attainable with a minimum effort of evaluating about few hundreds of features (note that the estimates of the true densities are based on the data obtained from samples containing $\approx 10^6$ cells and profiles.

### c) Estimation of planar and line characteristics

The estimated intensities $\lambda', \lambda''$ and their reciprocal values $\mathbf{E}a, \mathbf{E}l$ seem to be slightly biased and the above discussed loss of small profiles is at least partly responsible for it. Leaving the PVT section with thick lines aside, only one estimate from twelve (PG30) gives a lower value of the mean feature size. Hence the profile areas and chord lengths are systematically overestimated and the intensities are underestimated. It holds under the assumption that the magnitude of the bias $b$ is of the order of the difference between simulated values and values estimated by the measurement (Table 1) that for the tessellations A, B, C is $b([\mathbf{E}a]_{N_A}) \in (2,4)$ [%] of the correct feature size for the computerized analysis and $b([\mathbf{E}a]_{N_A}) \in (0,10)$ [%] for manual analysis. Similarly, $b([\mathbf{E}l]_{N_L}) \in (0,7)$ [%]. The range of this bias is $(12,26)$ [%] for the tessellation D.

On the contrary, the estimates of the factor $c$ seem to be unbiased (the bias of the both $\lambda', \lambda''$ has the same sign) and the difference $\Delta c$ between simulated and measured values is $0 \leq | \Delta c | \leq 14$ [%] which is an acceptable accuracy for the ratio estimator of $c$.

The inaccuracy in the estimates of the coefficients of variation CV $l$ and CV $a$ is surprisingly low. The only exception is the underestimate of CV $l$ in Bcf-0.2 by $-14\%$. Here the partial regularity of the section is a reasonable explanation. Otherwise, the difference between simulated and estimated values does not exceed 10% and the ratio 2:1 of underestimates to overestimates indicates only a small bias. This is much better result than in estimating mean values. The reliability of estimating coefficients of variations is an important result because they will be useful in the estimation of spatial characteristics.

### d) Estimation of spatial characteristics

Table 2 presents the estimates of $\lambda$ according to recommendations of the ASTM Standards ($[\lambda]_\bullet^{\mathrm{ASTM}}$) and by using the values of $c', c''$ obtained from simulations ($[\lambda]_\bullet$). The overestimation of $\lambda$ amounts to 25–40% for all but the BePS70 tessellation and is a necessary consequence of a considerable distance between the A, B, C points and the ASTM point in the $w$-$s$ diagram. In the case of BePS70 (D), the ASTM estimates give nearly correct values. However, it was already shown that the measured values of $N_A, N_L$ are heavily underestimated and thus the estimates again prove the positive bias of the ASTM approach and testify that two incorrect input values can produce a seemingly correct result.

Individual estimates using correct values of $c', c''$ amplify the inaccuracies in measured values because they are power function of $N_L, N_A$. Consequently, the

negative bias gradually increases with the growing inhomogeneity of tessellations. However, it does not exceed $-17\%$ for A, B, C tessellations.

The estimates of the coefficients of variation CV$v$ (Table 3) confirm the approximate validity of empirical equations within their above specified ranges. Reliable estimates were obtained for A, B tessellations (with one exception of $[\text{CV}_A v]_{\text{CV}_m l}$), acceptable underestimates for the C tessellation and only the order of magnitude estimates for the tessellation D lying far outside the range of the formulae validity.

Finally, it will be demonstrated in which way the $w$-$s$ diagram can be helpful in the common case X when neither the true spatial grain size nor correct values of $c'$, $c''$ are known. Then only the estimates of planar intensities and of planar coefficients of variance CV$_X a$ are known. As the spatial scale $\lambda = 1$ is unknown the recourse to scale invariant quantities is necessary and the factor $[c_X] = N_A/N_L^2$ is considered instead of the intensities. The situation is depicted in the Fig. 5. The examined samples A, B, C, D are represented by the dashed curves $c = c_A, \ldots, c_D$,
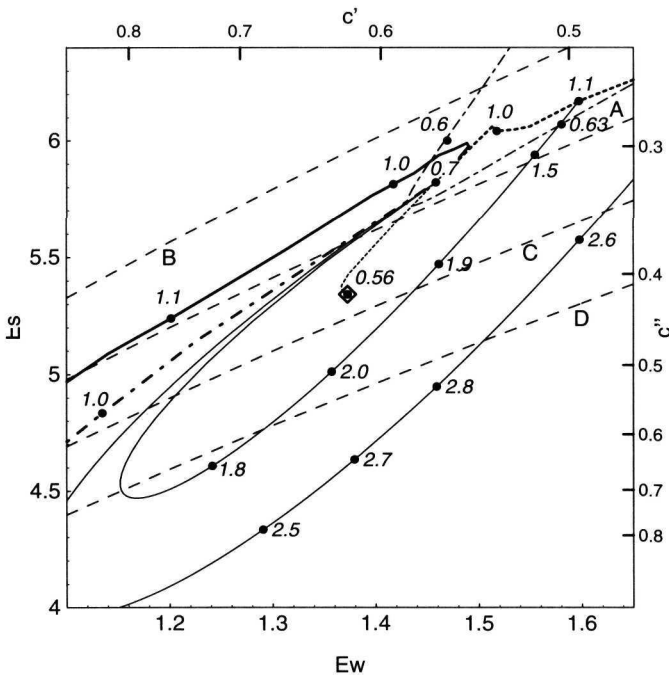


Fig. 5. The same part of the $w$-$s$ diagram as in Fig. 4 with the values of the coefficients of variation CV $a$ corresponding to selected tessellations and the dashed curves $c = \text{const.}$ for the estimated values $c_A, \ldots, c_D$ (Table 1) (denoted by A, B, C, D). The ASTM point lying close to the 1.0 point of the dash-dotted JM curve is omitted here. The point 0.63 in the right upper corner lies on the dash-dotted curve of hexagonal prisms; note that different values of CV $a$ can occur on different mutually intersecting curves.

e.g. $\mathbf{E}s = 4\sqrt{c_A \mathbf{E}w}$. The curves $\mathbf{E}s$ vs. $\mathbf{E}w$ representing various tessellations are plotted in Fig. 4 together with values of CV $a$ at selected points denoted by black circles. Thus CV $a$ increases when moving down along PG (thick full line) and JM (dash-dotted line) curves as well as when moving up along PS (thick dashed line) and Bcf (thin dashed line joining points 0.56 and 0.7, which correspond to rhombic dodecahedral tiling and PVT, resp.) curves. CV $a$ passes through a maximum when moving along BePS curves (thin full lines).

Now one can start to move down along the line A keeping in the mind the estimated value $\text{CV}_A a = 0.63$ (Table 1). At higher values of $\mathbf{E}w$, higher values of CV $a$ occur on the depicted curves. The value 0.63 can be expected somewhere near the intersection of the $c_A$ and Bcf curves, i.e. the point $[\approx 1.42, \approx 5.65]$ is tentatively assigned to the tessellation A and $c'_A = (\mathbf{E}w)^{-3/2} = 0.60$, $c''_A = (4/\mathbf{E}s)^3 = 0.35$ can be estimated in a reasonable agreement with the true values in Table 2. Similar arguments lead to the assignment D: $[0.6, 0.51]$ (the intersection of the $c_D$ curve with a line joining points with CV $a$ values 2 and 2.8 at the BePS curves). It gives $c'_D = 0.6$, $c''_D = 0.51$, again in a good agreement with Table 2.

The remaining two cases are less successful because of inaccurate values of $c_B, c_C$. The underestimated value of $c_B$ lies in the region of hexagonal prismatic tilings: their CV $a$ is $\approx 0.6$ at the tip of the curve and only very slowly increases in the upper branch intersected by the $c_B$ curve. Assigning tentatively B: $[1.5, 6.2]$, the estimates $c'_B = 0.54$, $c''_B = 0.27$ are obtained. These values would give small $(-6\%)$ underestimate of $[\lambda]_{N_A}$ and high $(-20\%)$ underestimate of $[\lambda]_{N_L}$. However, the estimated value of $\text{CV}_B a = 0.77$ is too high and the correct procedure would be perhaps to improve the estimates of the both $\text{CV}_B a$ and in particular $c_B$ by analysing more sections. The addition of three other sections ($\approx 200$ profiles and chords each of them) gives much better estimate $[c_B] = 0.67 \pm 0.02$.

Finally, the overestimated value of $c_C$ together with CV $a = 0.97$ would assign approximately the ASTM values of $c', c''$ to the sample C with the overestimates shown in Tab. 2. Again, the addition of three other sections gives $[c_C] = 0.73 \pm \pm 0.25$. It may be concluded that reliable estimates are strongly dependent on the accuracy of the estimates of the both CV $a$ and $c$. Approximately 1000 of grains and profiles is necessary to give a reliable estimate in sections with dispersed profile size (CV $a \geq 0.7$).

## 5. Conclusions

The main results of the present simulation study can be summarized as follows:

1. Reliable estimates of mean profile areas, mean chord lengths and corresponding coefficients of variances can be obtained with a moderate effort (only about 150–300 features examined) in grain structures with a low and medium grain volume dispersion (CV $a \leq 1$, CV $l \leq 0.7$). At a higher grain volume dispersion, the

loss of small sectional features is considerable and leads to a serious underestimation of their intensities. The accuracy of estimates by manual and high resolution image analysis is fully comparable.

2. The simultaneous application of profile and intercept counts can be used to reveal the deviations of the true scale independent factor $c$ from the values proposed by ASTM and other national standards. In particular, this deviation is of the order of $-10\%$ in structures with moderate grain volume dispersions.

3. By means of the $w$-$s$ diagram, the estimates of the factor $c$ and of the coefficients of variation CV $a$, CV $l$ may be used to improve the estimates of the 3D grain size intensity $\lambda$ obtained by the ASTM recommended approach, which systematically overestimates $\lambda$ if the grain volume dispersion is moderate.

### Acknowledgements

## REFERENCES

[1] VANDER VOORT, G. F.: In: Practical Applications of Quantitative Metallography. ASTM STP 839, ASTM, Philadelphia 1982, pp. 85–131.
[2] SAXL, I.—PONÍŽIL, P.: In: STERMAT'2000. Proc. Sixth Int. Conf. Stereology and Image Analysis in Materials Science. Eds.: Wojnar, L., Rożniatowski, K. Cracow, Polish Society for Stereology 2000, pp. 373, 379.
[3] STERIO, D. G.: J. Microsc., *134*, 1984, p. 127.
[4] OKABE, A.—BOOTS, B.—SUGIHARA, K.: Spatial Tessellations. Chichester, J. Wiley & Sons 1992.
[5] http://fyzika.ft.utb.cz/voronoi/
[6] SAXL, I.—PONÍŽIL, P.: Materials Characterization, *46*, 2001, p. 113.
[7] STOYAN, D.—KENDALL, W. S.—MECKE, J.: Stochastic Geometry and its Applications. New York, J. Wiley & Sons 1995.
[8] STOYAN, D.—STOYAN, H.: Fractals, Random Shapes and Point Fields. Chichester, J. Wiley & Sons 1994.
[9] SAXL, I.—PONÍŽIL, P.: Acta Stereol., *17*, 1998, p. 247.
[10] SAXL, I.—PONÍŽIL, P.: Appl. Math., *47*, 2002 (in print).
[11] MØLLER, J.: Adv. Appl. Prob., *24*, 1992, p. 814.
[12] HORÁLEK, V.: Materials Characterization, *25*, 1990, p. 263.